scientific reports

Check for updates

OPEN

Widefield ultra-high-density optical breast tomography system supplementing x-ray mammography

Miguel Mireles[1,5], Edward Xu[1,5], Morris Vanegas[1], Ailis Muldoon[2], Rahul Ragunathan[1], Shijie Yan[3], Bin Deng[2], Jayne Cormier[4], Mansi Saksena[4], Stefan A. Carp[2] & Qianqian Fang[1,3]✉

We report a wide-field compressive diffuse optical tomography (DOT) system – optical mammography co-imager (OMCI) – which aims to augment tens of thousands of existing x-ray mammography or tomosynthesis systems worldwide by adding functional assessment of breast tissue and improve cancer diagnosis. The OMCI system utilizes large field-of-view structured light illumination and single-pixel-camera based detection techniques to produce ultra-high spatial sampling density while ensuring that the inverse problem remains compact via the development of a unique target-adaptive pattern optimization technique to achieve compressive-sensing based measurements. The reconstructed images can be further enhanced by applying a compositional-prior-guided DOT reconstruction algorithm with tissue structural priors derived from a separately acquired x-ray mammography scans. In this report, we describe the design details and performance characterization of the imaging hardware as well as DOT image reconstruction pipelines. To validate this multi-modal breast DOT system, we include reconstruction results from both tissue-mimicking optical phantoms as well as clinical measurements from normal breasts obtained from a clinical study. Sample reconstructions from a breast containing a malignant tumor are also included, showing the potential of localizing and characterizing breast lesions using multi-modal measurements combining x-ray and DOT.

Breast cancer is the most common form of non-skin cancer in women in the United States, with an estimated 313,510 new cases in 2024 according to the American Cancer Society[1]. However, a steady decrease in breast cancer-related mortality rates has been observed since 1989, associated with the introduction of early diagnosis and routine screening protocols[2]. The most prevalent modalities used in clinics for breast cancer screening and diagnostics are x-ray full-field digital mammography (FFDM)[3], along with its three-dimensional (3-D) extension, digital breast tomosynthesis (DBT)[4], and ultrasound imaging[5]. These methods primarily characterize morphological changes associated with pathological tissue and, while being relatively low cost and widely accessible, have known limitations such as high false positive rates[6] and, in the case of FFDM and DBT, the use of ionizing radiation. Meanwhile, techniques such as contrast-enhanced magnetic resonance imaging (MRI)[7] and positron emission tomography (PET)[8] that assess tissue physiology have shown promise as more accurate diagnostic tools but are otherwise limited by cost, extended procedure times, and the use of radioactive or potentially toxic agents[9].

Diffuse optical tomography (DOT) utilizing non-ionizing near-infrared (NIR) light is an emerging technology that is capable of providing 3-D characterization of tissue physiology by means of the intrinsic optical contrast[10] of biological choromophores such as oxy- (HbO) and deoxy-hemoglobin (HbR) in a relatively low-cost, non-invasive, and safe platform. These characteristics make it particularly suited towards routine and longitudinal breast imaging[11]. However, the diffusive propagation of photons in the red and NIR regime in breast tissues[12], the typically coarse spatial sampling due to the use of discrete optical-fiber array based DOT systems, and their high susceptibility to tissue-optode coupling variations[13,14] lead to sub-optimal, low-spatial-resolution reconstructions of tissue chromophore maps[15], greatly impeding image interpretation and clinical adoption.

[1]Department of Bioengineering, Northeastern University, Boston 02115, USA. [2]Athinoula A. Martinos Center for Biomedical Imaging, Massachusetts General Hospital, Harvard Medical School, Charlestown 02129, USA. [3]Department of Electrical and Computer Engineering, Northeastern University, Boston 02115, USA. [4]Breast Imaging Division, Massachusetts General Hospital, Boston 02114, USA. [5]Miguel Mireles and Edward Xu contributed equally to this work. ✉email: q.fang@northeastern.edu

To address these limitations, researchers have turned towards multi-modal imaging, integrating high-resolution, anatomical imaging modalities such as structural MRI[16–19] and ultrasound[20] with co-registered optical scans from DOT. Over the past two decades, our group has been actively contributing to the development of multi-modal DOT breast imaging systems integrated with FFDM or DBT[21,22], with the key motivation that FFDM or DBT have broad availability worldwide, and have been routinely used as the gold-standard for breast cancer diagnosis and screening. We have investigated this approach in a series of studies including multi-modal DOT instrumentation design[22–24], x-ray prior-guided DOT image reconstruction algorithms[25–29], as well as clinical studies using co-registered DBT[21,24] or separately acquired FFDM images[30]. A clinical study accruing over 480 subjects had been conducted between 2005 and 2013 at Massachusetts General Hospital (MGH) for the systematic validation of a custom-built fiber-optics based DOT breast imaging system[24], demonstrating the potential of using spatially co-registered DBT and DOT to distinguish between malignant and benign breast lesions[21]. Despite these advances, the fiber-based optical probes has resulted in relatively coarse spatial sampling and difficulties in removing per-optode coupling variations[13,24], creating challenges in imaging small sized and early-stage breast tumors.

High-density DOT (HD-DOT) imaging systems have been actively explored to achieve improved tomographic reconstruction accuracy, especially in functional near-infrared spectroscopy (fNIRS) studies[31,32]. However, these reported HD-DOT systems still rely on discrete or fiber-optics coupled source and detectors. The increasingly complex and large-sized probes and elevated instrument costs impose limits upon further improvements in optical spatial sampling density. Measurements from individually coupled optodes also show susceptibility to optical coupling variations while requiring long data acquisitions.

Recent innovations in wide-field (WF) illumination and camera-based or single-pixel detection in DOT[33–35] offer dramatically increased spatial sampling density (by several orders of magnitude) as compared to state-of-the-art HD-DOT instruments, while simultaneously reducing the sensitivity to optode coupling variations as the area-based sources/detectors are relatively easy to calibrate. WF imaging confers additional benefits, including but not limited to accelerated data acquisition through the use of pattern illumination and compressive sensing, more uniform spatial sensitivity[36], and higher overall signal quality due to uniform spread of total illumination power, allowing for increased total source power without exceeding safety limits. Additionally, the use of camera-based single-pixel detection also opens the door for the development of data compression methods to form compact inverse problems without losing spatial information in the dense measurement data. Building upon recent advances in WF imaging in diffuse optics[37], our group has recently reported[36] that the use of multi-linear singular value decomposition (MLSVD) derived detection and illumination patterns can achieve DOT reconstructions with enhanced image contrast, reduced background artifact and accelerated computation.

Building upon our prior research, we introduce here a new generation of our DOT breast imaging system – an optical mammography co-imager (OMCI) – that has the potential to bring optics-based functional tumor assessment and, consequently, improved breast cancer characterization to tens of thousands of currently in-use and potential future clinical mammography scanners. The OMCI system utilizes dual-wavelength, wide-field, spatially-encoded illumination and camera-based detection to achieve both high-density spatial sampling and accelerated optical data acquisition for 3-D reconstruction of breast physiology while avoiding reconstruction artifacts resulting from unreliable tissue-fiber couplings. In addition, the OMCI system integrates a galvo-based frequency domain (FD) spectroscopy subsystem to account for the bulk tissue optical properties estimation and a structured light imaging (SLI) subsystem to acquire high-resolution 3-D breast surface shapes. These subsystems are leveraged in a x-ray mammography-like device that mimics the rotation and compression movements of commercial systems, making it possible to acquire DOT scans under a mammography-like breast compression and subsequently computationally register with a separately acquired 2-D FFDM or 3-D DBT x-ray mammography scan to perform multi-modal data fusion. In this work, we describe the OMCI imaging instrumentation design and the prior-guided DOT image reconstruction pipeline, along with the data compression techniques using breast-adaptive pattern optimization methods. We further validate the performance of the OMCI system through the reconstruction of heterogeneous optical phantoms measurements as well as experimental measurements in both normal and tumor-bearing breasts acquired through a clinical study.

Methods

OMCI instrument

An overview of the OMCI system is illustrated in Fig. 1a. The instrument integrates three optical imaging subsystems: (1) a galvo-based point-scanning frequency-domain (FD) system for determining absolute tissue bulk (i.e. volumetric average) optical properties, (2) an ultra-high-density, data-compressive, and wide-field CW imager for tomographic scanning of tissue physiology, and (3) a compact SLI shape acquisition system for obtaining breast 3-D surfaces for model-based image reconstruction. In addition, the OMCI system incorporates a motorized rotary table and a linear stage with a suite of sensors for breast compression and auxiliary monitoring. All these components are controlled and monitored using an in-house developed software. In the following sections, we present a detailed description of each of these modules.

In Fig. 1b, we provide a detailed diagram of the optical design of OMCI hardware, showing the optical components and light paths of the FD subsystem (green), CW subsystem (orange), and SLI subsystem (red). The FD and CW light sources are illuminated along the bottom plate below the compressed breast, made of a transparent acrylic sheet, with an electron-multiplying charge-coupled device (EMCCD) camera detector positioned above the compressed breast to capture the diffuse transmitted light from the top surface of the breast as CW measurements as well as an optical fiber clipped on the upper plate for capturing FD optical data.

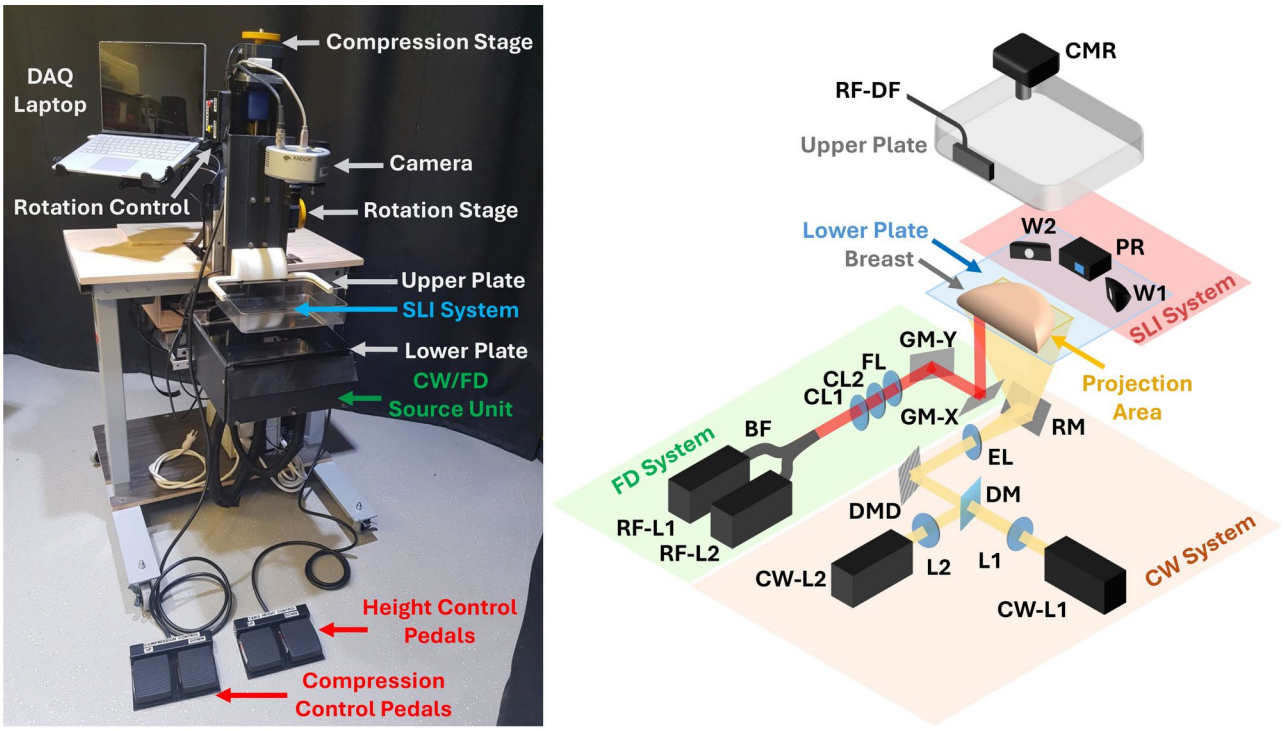

Fig. 1. The OMCI system, shown as (**a**) a photo of the imaging hardware, including an optical imaging assembly containing a camera on top and the source unit at the bottom, an articulating data acquisition laptop, and foot-pedals and motor controllers for applying mammography-like compression, height adjustment and rotation. In (**b**), we also include a detailed schematic depicting the components in the OMCI optical imaging subsystems. The continuous-wave (CW) imaging subsystem includes two CW lasers (CW-L1/2), lenses (L1/2), a dichroic mirror (DM), a digital micromirror device (DMD), an expansion lens (EL), a reflection mirror (RM), and the measuring camera (CMR). The frequency-domain (FD) imaging subsystem consists of two radio-frequency-modulated lasers (RF-L1/2), a bifurcated fiber bundle (BF), collimation lenses (CL1/2), a focusing lens (FL), dual-axis galvo mirrors (GM-X/Y), and a detection fiber (RF-DF) located above the imaging target. The structured light imaging (SLI) subsystem consists of two webcams (W1/2) and a pattern illumination projector (PR).

Galvo-based frequency-domain subsystem

To recover absolute tissue bulk optical properties, the OMCI system incorporates a compact, single-detector-channel FD spectroscopy scanner based upon a frequency-multiplexing strategy[38], highlighted in green in Fig. 1b. Briefly, the FD subsystem consists of two laser modules (RF-L1/L2) illuminated simultaneously at 685 and 830 nm (Thorlabs Inc., NJ) and modulated at 67.5 and 75 MHz, respectively, each with 20 mW mean output power. Each laser module is coupled to one 400 μm core input fiber of a custom-built bifurcated fiber bundle (BF) and the dual-wavelength source beam emitted from the bundled fiber is focused to a 5 mm diameter spot at the surface of the bottom compression plate through a series of optical lenses (C610TME-B, LA4647-B and AC254-300-B, Thorlabs Inc., NJ). A dual-axis galvo-mirror (GM-X/Y) system (GVS002, Thorlabs Inc., NJ) is used to steer the dual-wavelength source beam to 14 positions along a 6 cm linear path parallel to the plate edge next to the subject's chest wall; the laser power delivered to the breast surface is 11 mW and 6 mW at 685 nm and 830 nm, respectively. An additional dwelling position is located on a light-absorbing fabric (BFP1, Thorlabs Inc., NJ) to acquire the "dark reading". The transmitted diffuse light from both wavelengths is collected by a 2.5 mm diameter detection fiber bundle (RF-DF), which is attached to the top compression plate via a 3-D printed mount positioned directly above the outermost source position. The top-compression paddle has an inward offset about 2 cm from the edge of the bottom compression plate, adding a minimum spacing between the imaging domain from the chest wall tissues. The galvo-scanned FD source illumination positions extend further by ~1 cm in the direction of the nipple to minimize the impact of the chest wall. Detected light signals are then transferred to an avalanche photodiode detector (C5331-04, Hamamatsu, Japan) in the FD detection module to undergo demodulation to acquire the amplitude and phase of the FD signals. The dwell time at each of the 15 galvo scanning positions is 2 s, with an additional 200 ms between measurements to account for the time to switch between positions. With a 90 Hz FD data sampling rate, the FD subsystem averages 180× amplitude and phase data samples to obtain a single complex-valued FD measurement data point for each wavelength at every position. The total FD data acquisition time is around 35 s. Assuming an average compressed breast thickness of 6 cm, the source-detector (SD) separation ranges from 6 to 8.5 cm.

Ultra-high-density wide-field tomography subsystem

The wide-field (WF) continuous-wave (CW) imaging subsystem, shaded in orange in Fig. 1b, utilizes a customized projector (P300 Neo, AAXA Technologies, USA) for dual-wavelength illumination, coupling two laser modules at 660 nm (CW-L1, 125 mW emitting power) and 830 nm (CW-L2, 100 mW emitting power) to the digital micro-mirror device (DMD) of the projector using a dichroic longpass filter (69-882, Edmund Optics, USA). The two wavelengths are temporally multiplexed and controlled using a microcontroller (Arduino UNO, Arduino, Italy) that interfaces with the OMCI control software. The modified projector produces a full illumination area of $11\times6\ \mathrm{cm}^2$ at the surface of the bottom compression plate with a total output power of 30 mW ($0.45\ \mathrm{mW/cm}^2$) at 660 nm and 10 mW ($0.15\ \mathrm{mW/cm}^2$) at 830 nm. Light transmitted through the imaging volume is collected by a 14-bit EMCCD camera (CMR, Andor Luca R, Oxford Instruments, U.K.) with a 12 mm, f/1.4 objective lenses (MVL12M23, Thorlabs Inc., NJ) positioned about 45 cm above the top compression plate. A total of 34 illumination patterns are sequentially projected at each wavelength, including a set of 32 illumination patterns, plus a full-white (all-one) and a full-black (all-zero) pattern. Images are acquired using a 200 ms exposure time per illumination pattern, from which single-pixel readings are computed[39,40].

In addition, the EMCCD camera offers programmable electron-multiplying (EM) gain settings to significantly boost low-light measurements. We employ the bisection method to automatically identify the most appropriate EM gain settings for a given imaging target at the start of each scan by projecting one of the sliding bar patterns closest to the center of the camera's field-of-view, where the measurement intensity is typically the highest, and adjusting the EM gain until the average reading from an acquired image is within 15-20% below the saturation threshold of the camera, which has been empirically tested to minimize camera saturation across all images while optimizing overall signal quality. This process is repeated for each wavelength and images are acquired at the same exposure (200 ms) used during experimental data collection, with the bisection search starting with the lower and upper bound of the EMCCD camera's gain settings (0 and 200, respectively). All evaluated EM gain levels and their corresponding images are saved, from which we compute an EM gain correction factor for image calibration. This process requires 3-5 s per wavelength, acquiring on average 10-15 images, and is automated by the OMCI software using the application programming interface (API) tools for Andor cameras.

Breast shape scanning subsystem

A detailed description of our low-profile structured light imaging (SLI) system for breast 3-D shape acquisition and its calibration procedure can be found in our previous publication[41]. Briefly, this dual-camera SLI system is mounted on the bottom compression plate and pointed towards the breast. It consists of a central projector (PR, AAXA Technologies, USA), casting a total of 38 complementary gray-code bar patterns[42] onto the breast, and two webcams (W1/2, Logitech, Switzerland) located on each side of the projector to acquire images of each illumination using a 250 ms exposure time. During data acquisition, the brightness of the SLI illumination is dynamically adjusted to accommodate different skin tones and breast sizes while preventing saturation and reflections from the compression plates.

Breast compression mechanical system and auxiliary sensor suite

The OMCI system is capable of performing mammography-like breast compression. This is achieved using a combination of a linear (Velmex Inc., USA) and a rotary (LinTech Motors, CA) translation stage, each actuated by a stepper motor and controlled through a motor driver interface (Velmex Inc., NY). To mimic clinical mammography systems, the OMCI system is equipped with a pair of foot pedals and buttons to adjust rotation angles, compression, and table height (Fig. 1a). In addition, a suite of mechanical sensors, including 2× limit switches (Velmex Inc., NY), a reed switch in the rotary stage (LinTech Motors, CA), 4× load sensors (SparkFun, CO), and a linear encoder (ETI Systems, CA) provides auxiliary information for confining the mechanical stages and measuring both compression pressure and breast thickness.

Optical system characterization and phantom validation

To characterize the FD subsystem, the source and detection fibers are coupled to a dual-axis filter wheel (Thorlabs Inc., NJ) with 36 levels of attenuation using combinations of neutral-density filters with optical densities (OD) ranging from 0 to 6.70 at 685 nm and 6.15 at 830 nm. A total of 180 FD data samples are collected over a duration of 2 s for each attenuation level, from which the noise equivalent power (NEP), defined as the signal power at which the signal-to-noise ratio (SNR) is equal to one, and the dynamic range for both amplitude and phase can be determined. In addition, inter-wavelength cross-talk is evaluated by comparing measurements for both wavelengths simultaneously against those with only 685 or 830 nm illumination.

Characterization of the CW subsystem is performed using a homogeneous slab phantom of known optical properties ($\mu_a = 0.006\ \mathrm{mm}^{-1}$, $\mu_s' = 0.84\ \mathrm{mm}^{-1}$ at 660 nm and $\mu_a = 0.005\ \mathrm{mm}^{-1}$, $\mu_s' = 0.53\ \mathrm{mm}^{-1}$ at 830 nm). With the phantom positioned over the illumination area and the compression plates adjusted to the thickness of the phantom, a set of 32 sliding-bar[39,40] illumination patterns are projected onto the bottom surface of the phantom. To evaluate the effect of EM gain on image intensity, we repeat this process while incrementally adjusting the EMCCD camera EM gain by 5 to acquire data at 5 levels: 0, 5, 10, 15 and 20; for each EM gain setting, 10× repetitions of images are acquired for each illumination pattern. Single-pixel (SP) measurements are then computed by integrating with either the sliding-bar or target-adaptive detection patterns[36]. The means, standard deviations, and signal-to-noise ratios (SNR) of the acquired signal are then evaluated across the 10 repetitions for each detection pattern set for every EM gain setting.

Phantom and clinical experiment protocols

Optical phantom experiments are performed to validate the imaging performance of the FD and CW optical subsystems. Measurements are acquired from two different silicone-based optical slab phantoms – a

homogeneous phantom for system calibration, and a heterogeneous phantom with two spherical inclusions (15 and 20 mm in diameter, respectively, both with a 2.3× absorption contrast). Images are then reconstructed following the workflow outlined in Section Data analysis. The SLI system is not used as part of this experiment due to the known geometries of the slab phantoms.

The human subject study was conducted at the Massachusetts General Hospital under protocol 2018P000451 approved by the Mass General Brigham Institutional Review Board (IRB) which considered the principles of the Declaration of Helsinki as well as additional rules and regulations as required by the US federal government and local authorities. The research was performed in accordance with all relevant guidelines and regulations. Written informed consent was obtained from each subject prior to initiating the study procedures, which consisted of a bilateral optical breast scan. We also retrieved the subject's most recent x-ray FFDM images if any were available within the previous 6 months before the experiment date to use in our image analysis.

For clinical optical data acquisition, the vertical linear stage in the OMCI system is first adjusted to match the subject's height in standing position; the rotational stage is then adjusted using the motor controller to create a mediolateral-oblique (MLO) compression angle. The linear stage controlling the breast compression is then set to the fully-released position before the operator positions the subject's breast between the two compression plates and applies compression according to clinical conventions for breast mammography. A light-absorbing fabric (Thorlabs, NJ) is padded around the breast between the two compression plates, minimizing stray-light from the environment. With the room-light turning off, an automated FD/CW data acquisition is performed. The OMCI system acquires dual-wavelength FD data at 15 positions (around 35 s), followed by sequential CW acquisition at 660 and 830 nm, each consisting of a rapid (< 5 s) EM gain optimization and a full set of 32 pattern projections, a full-white image, and a full-dark image over a span of about 15 s. Once the FD/CW scan is completed, the operator removes the light-absorbing fabric padded around the breast and acquires the 3-D breast shape using the SLI system. This acquisition takes about 35 s to complete. The subject's breast is released from compression following the completion of acquisition and we subsequently repeat the above procedure to image the contralateral breast. The total compression time for each breast is between 3 to 4 minutes, comparable to our previous clinical studies[21]. A homogeneous slab-shaped silicone phantom with tissue-like optical properties (μ_a =0.005 mm^{-1}, μ_s'=1.3 mm^{-1} at 660 nm) is imaged using similar protocols following the clinical measurement and used later for data calibration.

Data analysis

A schematic of the data analysis pipeline describing the processing steps of the multi-modal data acquired by each of the sub-system is shown in Fig. 2 and is explained in detail in the following sections. We note that most of these processing steps have been automated to minimize manual operator intervention. All forward and inverse modeling is performed using our in-house, open-source diffusion solver, Redbird-m[43].

Breast surface acquisition and mesh generation

The images acquired from each SLI camera are processed using the Scan3d-Capture toolbox[44] to generate point clouds, which are then co-registered using a least-square minimization procedure constrained by a top-down image of the breast captured by the EMCCD camera [see Fig. 3a]. The merged point cloud from both cameras is converted into an open triangular surface using a Poisson surface reconstruction[45] and then repaired to form

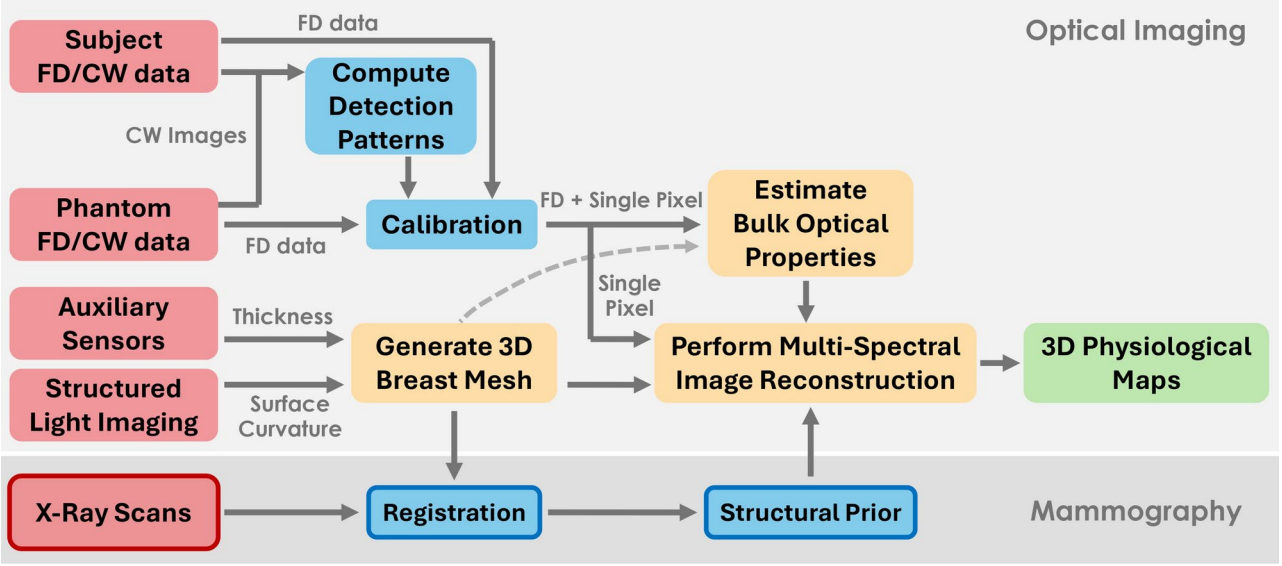

Fig. 2. Schematic for the multi-modal OMCI data processing pipeline. For human subjects, the x-ray mammography and optical scans are separately acquired, co-registered and used jointly in image reconstructions. All steps are color-coded: red for raw data, blue for pre-processing, yellow for image reconstruction, and green for output.

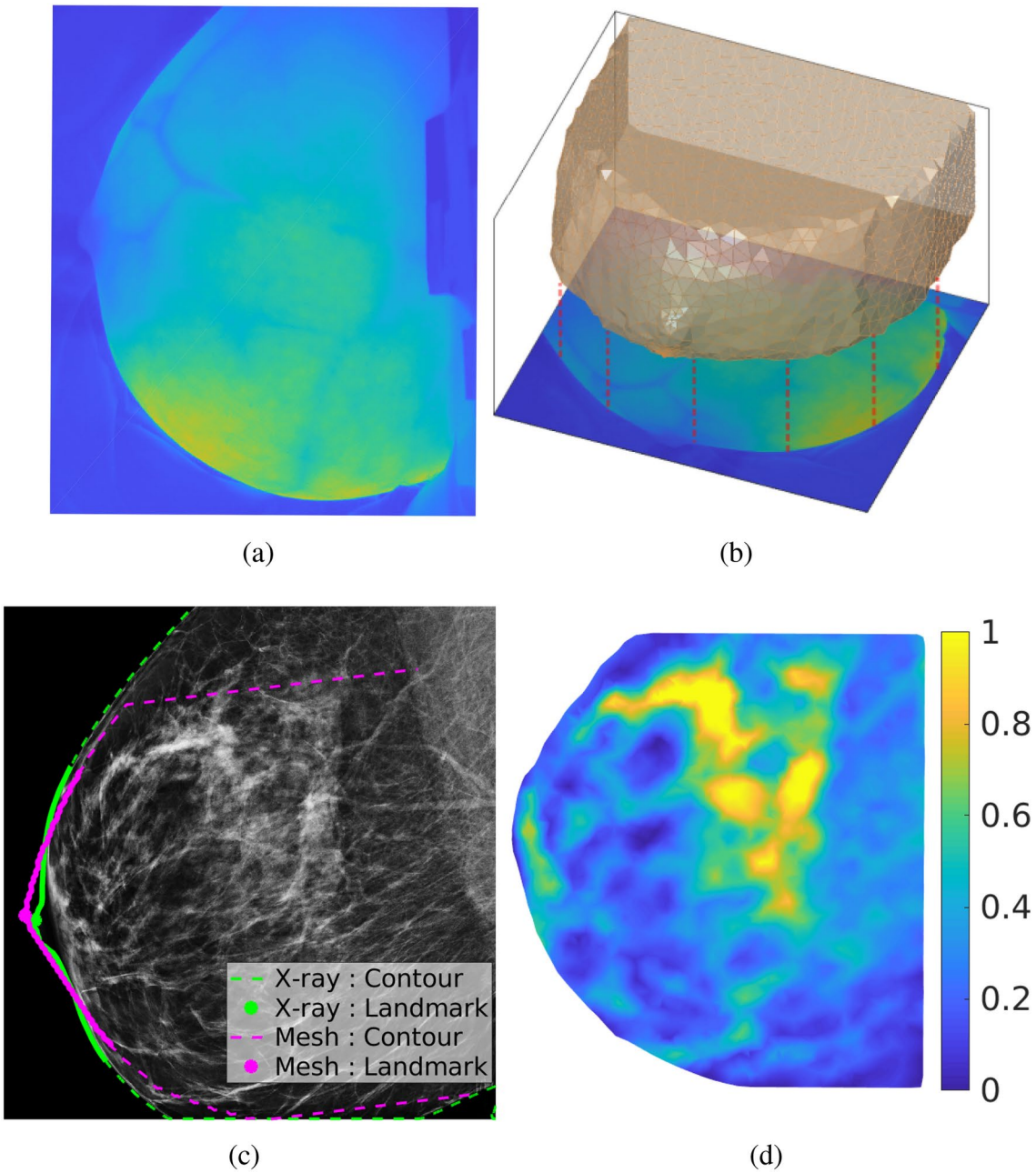

Fig. 3. Example optical and x-ray images acquired from a normal breast, showing (**a**) diffuse transmittance image using full-white illumination acquired by the camera, (**b**) a tetrahedral breast mesh co-registered with the camera image, (**c**) separately acquired mammogram of the same breast, with co-registered breast contours extracted from the breast mesh (magenta) and mammogram (green), and (**d**) compositional prior of the fibroglandular tissue (as volume fraction) derived from the mammogram. The breast contour registration is performed using an iterative closest-point (ICP) algorithm by matching the solid-line portions from both the x-ray and mesh derived contours.

a closed 3-D surface [see Fig. 3b] using a MATLAB based mesh generation toolbox Iso2Mesh[46,47]. The breast 3-D surface is extended towards the chest wall direction by 2 cm to minimize boundary effects due to mesh truncation. Finally, the surface is tessellated into tetrahedral volumetric meshes at two density settings: a high-density mesh at a maximum element volume V_{max} = 10 mm^3 to compute forward solutions and a coarser one (V_{max} = 15 mm^3) as the reconstruction mesh to store the recovered optical parameters.

X-ray and optical data registration and compositional priors

For each measured subject, a previously acquired 2-D FFDM mammogram imaged in the MLO view following similar compression protocols is retrospectively obtained within the 6 months prior to the optical scan date, allowing for both the interpretation of the optically recovered physiology maps and the generation of structural

priors for enhanced DOT reconstructions. To register the 2-D mammogram to the 3-D breast model, the contour line of the breast is extracted from the tetrahedral mesh along the z-plane where the breast is widest along the chest wall to nipple direction, shown in magenta in Fig. 3c. Similarly, the contour line of the breast from the mammogram is also extracted (green lines in Fig. 3c) and scaled according to the mammogram pixel size. The respective nipple position (shown as green/magenta disks) from each of the two contour lines is manually selected. Curved segments of the breast contours spanning 5 cm in either direction from the nipple (solid line segments in Fig. 3c) are then used to compute the affine transform for mapping the mesh to the mammogram using an iterative closest point (ICP) algorithm[48].

A compositional-prior guided DOT reconstruction technique[25,26,30] is applied for jointly considering x-ray structural and optical information within the DOT reconstruction framework. The regularization matrix encoding structural priors is created using probabilistic maps of the fibroglandular and adipose tissues derived from the mammogram image using a linear-mixing model[26], with the fibroglandular tissue fraction shown in Fig. 3d. Because the resolution of x-ray imaging is significantly higher than the number of nodes within a mesh, each node's respective gray-scale value is computed as an average of pixels falling within a $2.5\times2.5\ \mathrm{mm}^2$ area around the node.

System calibration and data pre-processing

Prior to acquiring experimental data, a system characterization measurement is performed to identify the locations of the illumination patterns, the FD sources, and detector fiber. This is achieved by placing a diffusing surface, usually a sheet of white paper, over the illumination area on the bottom compression plate while the top plate is fully compressed (i.e. in direct contact with the bottom plate). The 15× FD source positions per wavelength (a total of 30), 32× CW patterns per wavelength, a full-white CW pattern for each wavelength, along with a line indicator displayed from the CW projector aligned with the FD detection fiber position, are sequentially illuminated and the images are captured using the EMCCD camera. From these images, the information needed for image reconstructions in the next step are automatically extracted.

In addition, a full optical scan, including both FD and CW data, of a homogeneous phantom (referred to as reference or "R") of known optical properties is acquired and used to calibrate the measurements from subsequent breast imaging experiments (referred to as target or "T"). For CW data pre-processing, we first compute a factor, α, to correct for the respectively-optimized EM gains at which reference and target images are acquired at, denoted as g_R and g_T, respectively. To do so, the averaged image intensity values $[I_R(g)]$ from the non-saturated images acquired from the reference phantom and their respective EM gain values (g) are used to fit a linear model, $\Gamma(g)$; α is then defined as the ratio between target and reference images acquired at the same EM gain and computed as $\alpha = \frac{I_T(g_T)}{\Gamma(g_T)}$, where $I_T(g_T)$ is the averaged image intensity value for the target domain at the optimized EM gain and $\Gamma(g_T)$ is the image intensity value for the reference phantom at g_T evaluated using the linear model. For FD measurements, α is set to 1 as the FD detector does not use EM gain. Finally, the FD and CW optical data are calibrated using the following equation:

$$\Phi_T' = \alpha \frac{\Phi_T}{\Phi_R} \Phi_S$$

where Φ_T' is the calibrated FD or CW measurement from the target; Φ_T and Φ_R are the raw experimental target and reference phantom measurements, respectively, from the FD/CW system, and Φ_S represents the simulated FD/CW forward model using the known optical properties and shape of the reference phantom.

Although our EMCCD camera-based detection offers high density scans (1004×1002 pixels, with an estimated pixel size of 0.16 mm) of the diffusely transmitted CW light in a large field-of-view, solving the inverse problem using per-pixel measurement is computationally prohibitive due to the sheer size of the linear system needed for the inversion. Instead, we adopt a "digital" single-pixel camera (SPC) approach by multiplying each detected camera image by a set of basis functions, referred to as the "detection patterns" and sum such pattern-weighted images to form a single-pixel (SP) measurement per detection pattern. This is equivalently to applying a detection pattern over the detector DMD in an SPC system[49]. A number of choices of detection patterns have been investigated[36]. In this work, we compare results from two sets of detection patterns: (1) sliding-bar patterns that mirror the illumination patterns, and (2) multi-linear singular value decomposition (MLSVD)-based target-adaptive patterns derived following the methods described by Mireles *et al.*[36]. We particularly highlight here that the use of detection patterns produces a highly compact inverse problem without losing the spatial information from the pixel-wised camera raw data.

To ensure that the SP values effectively captures the spatial information from the camera images, the camera acquired images are cropped by the intersections between two contours: (1) the bounding rectangle of the top surface of the target, and (2) a rectangular area extended 15 mm outside of the source illumination area (except the edge nearest to the chest wall). The detection patterns are stretched to match the cropped image space before multiplication to ensure all source/detection channels contain optical information.

Bulk property estimation and image reconstruction

Following a workflow previously described in Fang et al.[24], we perform a multi-spectral DOT reconstruction using an iterative Gauss-Newton reconstruction with Tikhonov regularization to recover the 3-D distribution of physiological parameters (HbO, HbR) in a two-step process. First, bulk optical properties (μ_{a0} and μ_{s0}') are recovered using both FD and CW measurements jointly[24], providing accurate estimates for the bulk optical properties of the breast tissue being scanned. These bulk optical properties then serve as the initial guess for the subsequent tomographic image reconstruction. We obtained reconstructed images comparing two detection

patterns – sliding-bar and MLSVD-optimized patterns, also with and without anatomical priors. For prior-guided image reconstructions, the registered x-ray anatomical information is incorporated as part of the regularization matrix of the DOT reconstruction[25]. The regularization parameter λ is determined for each reconstruction in the first iteration using the L-curve[50] method.

Results

OMCI imaging hardware performance characterization

Frequency-domain sub-system characterization

The performance of the built-in FD subsystem is largely in agreement with our previously reported results[38] using the same architecture. The noise equivalent power (NEP) is measured at 6.0 pW/$\sqrt{Hz}$ and 5.7 pW/$\sqrt{Hz}$ for 685 nm and 830 nm wavelengths [Fig. 4a], respectively, while the phase noise [Fig. 4b] is quantified to be less than 10 mrad/$\sqrt{Hz}$ in each wavelength at optical powers higher than the 100 pw incident power. A dynamic range greater than 100 dB (20 $\log_{10}$) for both wavelengths is characterized when reaching the saturation level of the detection sensor at 1.5 μW. Additionally, the system stability is assessed over a time period of 20 minutes of continuous data acquisition. A variance of less than 1 % was observed in both amplitude and phase results. No inter-wavelength or amplitude-phase cross-talk is observed during this period.

Continuous-wave wide-field sub-system characterization

To facilitate the comparison of overall signal quality, we plot in Fig. 5 the single-pixel (SP) data intensity (in $\log_{10}$-scale) and SNR (in dB) at 660 nm with the data points sorted in descending order (along the dimension of detection pattern index) per every source pattern. We also repeat such plot at 5 EM gain settings: 0 (black), 5 (blue), 10 (red), 15 (green) and 20 (magenta). When comparing signal qualities using sliding-bar patterns (a,b) and those produced using MLSVD-optimized patterns (c,d), the former results in overall lower intensity and lower average SNR compared to the latter; about 20% of the sliding-bar derived SP measurements also show a rapid degradation in both intensity and SNR, resulting from spatially distant sliding-bar patterns and the sparse nature of the bar patterns. The average SNR for MLSVD-optimized patterns at EM gain levels of 0, 5, 10, 15, and 20 are 65.2 dB, 70.4 dB, 71.0 dB, 71.3 dB and 72.3 dB, respectively, compared to 61.3 dB, 65.3 dB, 65.8 dB, 66.0 dB, and 66.4 dB when using sliding-bar patterns. In comparison, the MLSVD-optimized detection patterns show relatively uniform intensity and SNR (between 60-80 dB) readings as well as overall elevated SNR as the MLSVD patterns generally cover the entire detection area (see Fig. 2 in Mireles *et al.*[36]). Similar observations have been made for 830 nm (not shown). Measurements acquired at different EM gains at 0, 10, 20, and 30 and generally show linearly increased intensity and improved SNR.

Validation using optical phantoms

Reconstructed images for the silicone phantom with inclusions using both sliding-bar and MLSVD-based adaptive patterns [Fig. 6a,b] show successful recovery of the two inclusions at the expected locations. In Fig. 6c, we also plot the cross-sections of the aforementioned images at $y = 52$ mm (blue) and $y = 66$ mm (red), centered at the left-upper and right-lower inclusions, respectively. The recovered full-width half maxima (FWHM) are similar for both sliding-bar and medium-adaptive detectors, 23 and 22 mm for the smaller (15 mm) inclusion, respectively, and 28 and 29 mm for the larger (20 mm) inclusion. Meanwhile, medium-adaptive detection patterns confer slight improvements in reconstructed contrast (1.72× and 1.86× for the smaller and larger inclusions) when compared to sliding-bar detection patterns (1.63× and 1.73×). These enhancements are also supported by a lower (about 3%) measurement residual [Fig. 6d], computed as the error between the calibrated

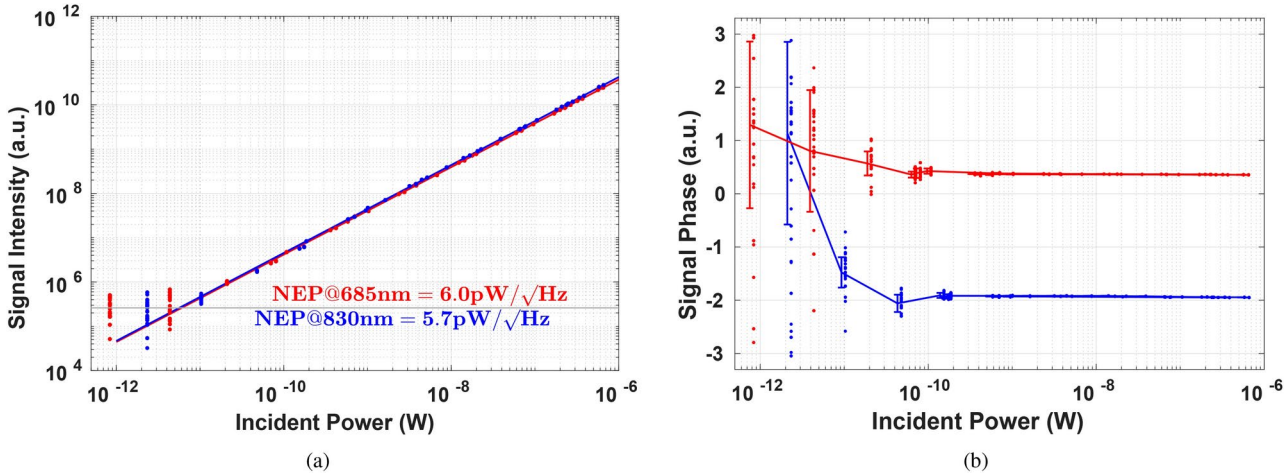

Fig. 4. Characterization of the frequency-domain (FD) subsystem at 685 nm (red) and 830 nm (blue), including (**a**) amplitude in log-scale versus incident optical power, revealing a noise equivalent power (NEP) of around 6 pW/$\sqrt{Hz}$ at both wavelengths, and (**b**) phase versus incident optical power.

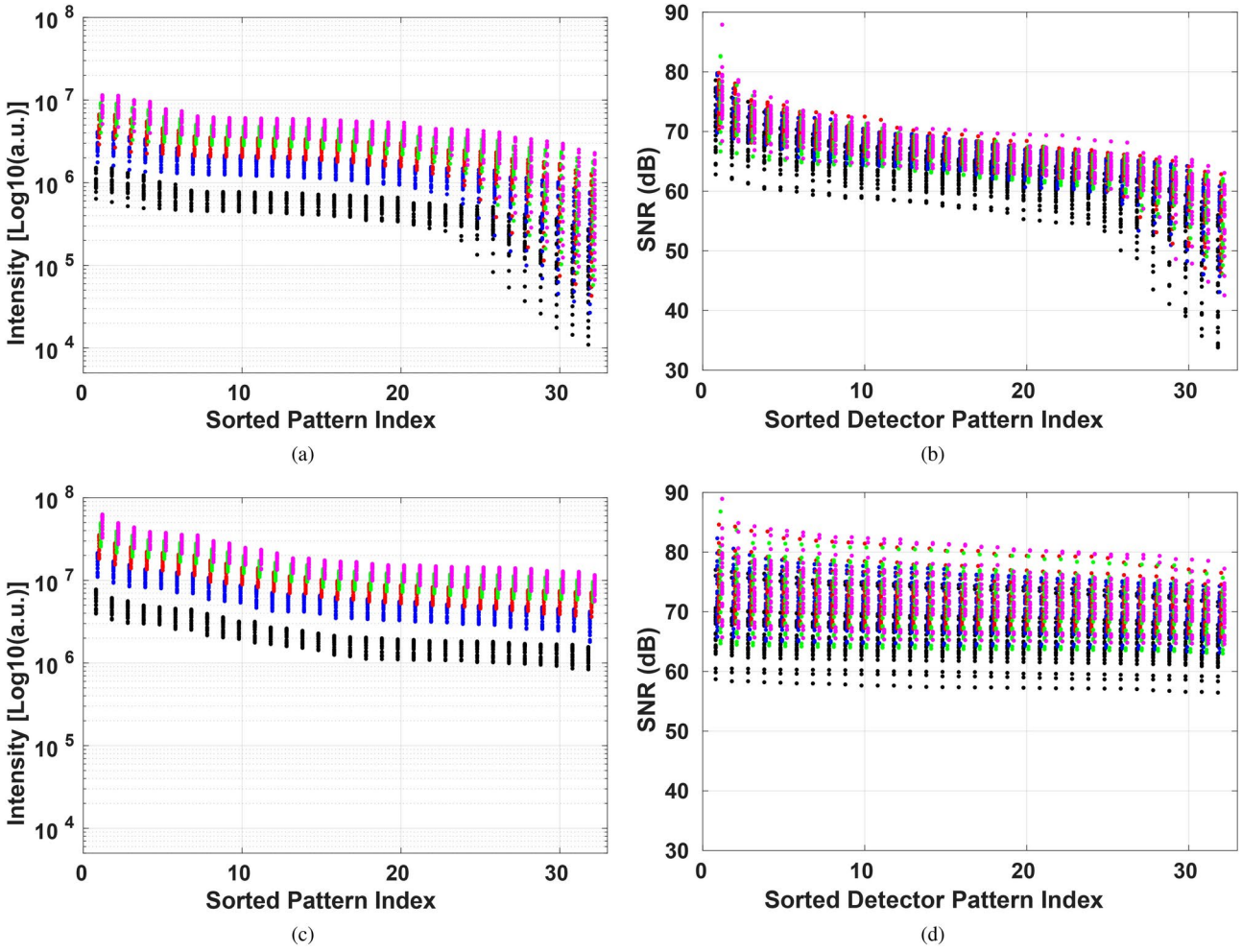

Fig. 5. Characterization of the continuous-wave (CW) subsystem at 660 nm using 10 repeated phantom measurements. Signal intensities (**a**,**c**) and single-pixel measurement signal-to-noise ratios (SNR) (**b**,**d**) are sorted in descending order for each illumination pattern and plotted against the sorted detector pattern index using either sliding-bar (**a**,**b**) or MLSVD-optimized (**c**,**d**) patterns. Colors represent electron-multiplying (EM) gain settings: 0 (black), 5 (blue), 10 (red), 15 (green) and 20 (magenta).

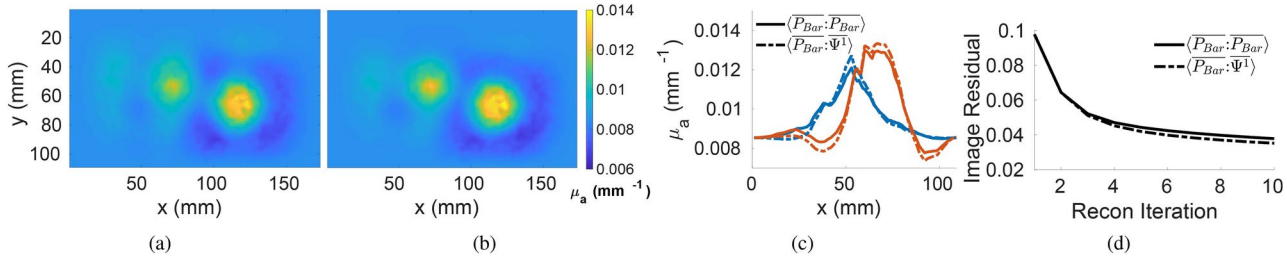

Fig. 6. Experimental phantom validation of the OMCI system. The recovered absorption coefficient (μ_a in mm^{-1}) images at the $z = 26$ mm plane are shown for a phantom of 52 mm thickness containing two optical inclusions using (**a**) sliding-bar detection patterns and (**b**) MLSVD-derived patterns. The cross-sectional plots at $x = 71$ mm (blue) and 117 mm (red) for each detection pattern type are shown in (**c**). The diffuse transmittance image residuals, which compute the differences between calibrated detector (camera) measurements and simulated detector measurements, obtained by solving the forward model of the reconstructed domain at each iteration, are plotted against reconstruction iterations in (**d**) and show the convergence of the reconstruction.

experimental wide-field images and the simulated wide-field diffuse transmittance at the detector z-plane for each iteration of the reconstruction, for the optimized bar patterns results.

Clinical validation of OMCI system

We have acquired bilateral optical breast scans with the OMCI system from N = 21 subjects following the protocols described in Sections 2.4.1- 2.4.4. The estimated averaged bulk total hemoglobin (HbT) is 23±8 μM whereas the mean oxygen saturation (SO_2 = HbO/HbT) is 0.62±0.05. Moreover, HbO and HbR are of 14.6±6.1 and 8.4±2.1 μM, respectively. These physiological quantities are comparable to our previously reported results[21] using a fiber-based DOT system.

A sample set of the recovered total hemoglobin concentration (HbT in μM) images of 3 breasts from 2 healthy subjects with ages ranging from 44 to 54 years old are shown in Fig. 7, alongside with their corresponding 2-D mammograms (1st column). In this plot, we also compare between four image reconstruction settings, including the non-prior-guided HbT image cross-sections using sliding-bar detection pattern (2nd column) and those using MLSVD patterns (3rd column), as well as x-ray prior-guided HbT images using sliding-bar (4th column) and MLSVD patterns (5th column); all of them use sliding-bar patterns for illumination. Finally, we also plot the residuals between measured and computed diffuse transmittance images over various iterations of reconstructions (6th column) and compare the convergence between various reconstruction settings. A total iteration number of 10 was empirically selected to yield steady residuals in most tested phantom and human data reconstructions.

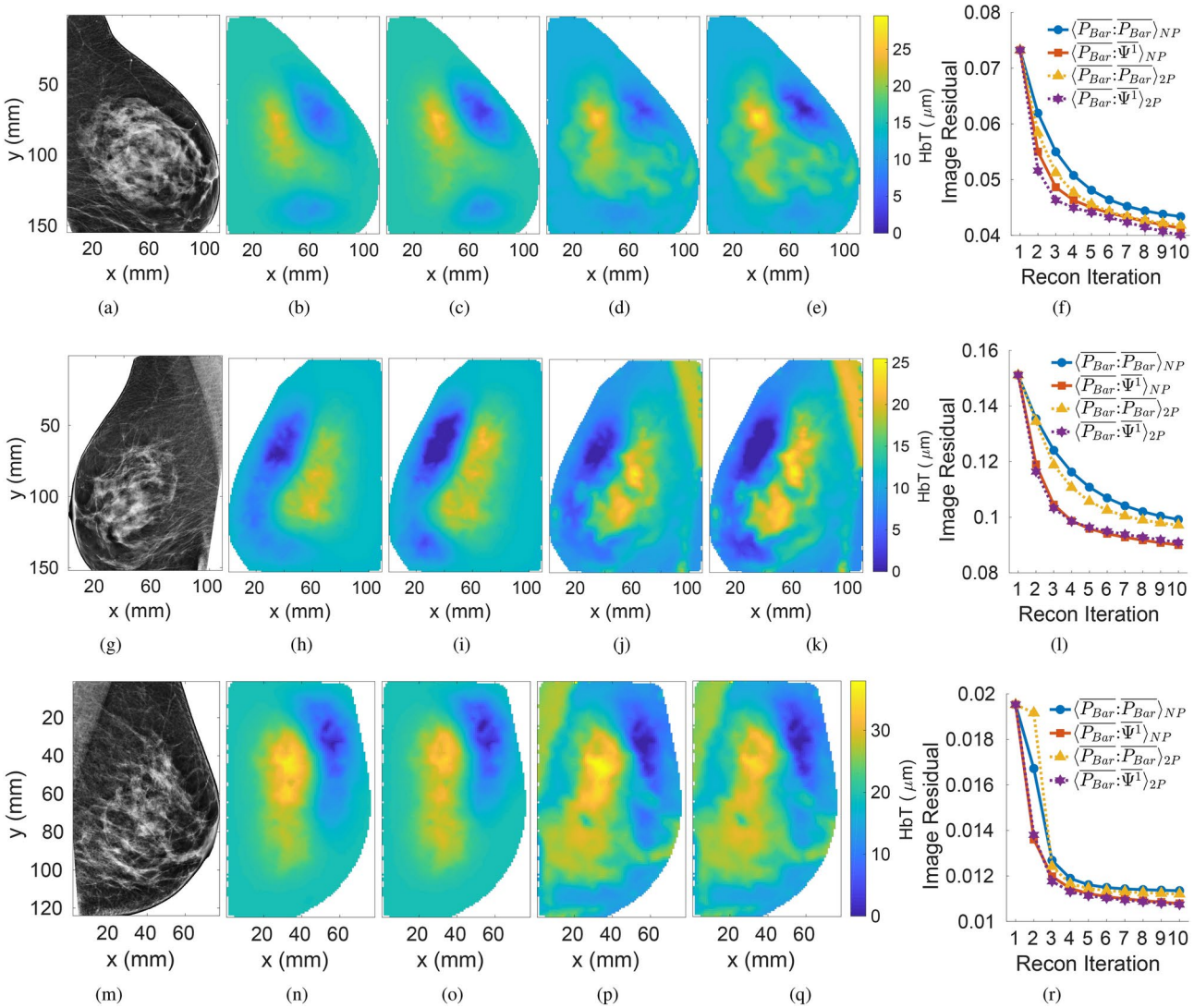

Fig. 7. Example reconstructed total hemoglobin concentrations (HbT) from clinical breast measurements. For each breast, we show the registered x-ray mammogram (**a**,**g**,**m**), non-prior-guided HbT using (**b**,**h**,**n**) sliding-bar and (**c**,**i**,**o**) MLSVD detection patterns, as well as their prior-guided counterparts in the 4th (**d**,**j**,**p**) and 5th (**e**,**k**,**q**) columns, respectively. In the last column (**f**,**l**,**r**), we plot the diffuse transmittance residual over reconstruction iterations comparing the convergence behaviors of different reconstruction setting.

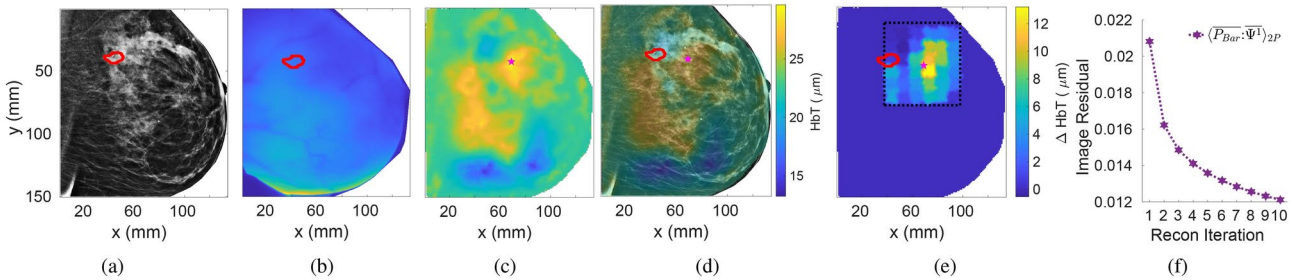

Fig. 8. Reconstructed images from a breast containing a 10 mm diameter invasive ductal carcinoma (IDC), including (**a**) the mammogram of the breast, (**b**) a diffuse transmittance image acquired by the OMCI EMCCD camera, (**c**) the cross-sectional image of the recovered HbT at $z = 30$ mm using only the adipose and fibroglandular compositional priors and MLSVD-derived detection patterns. We also show the overlay of the HbT image with the x-ray mammogram in (**d**) along with the image residual over reconstruction iterations (**f**). In (**e**), we show the ΔHbT images assembled from 6×6 image reconstructions – for each reconstruction, the maximum HbT difference between the image recovered with and without assuming a tumor in the center of the search grid, is displayed over the nodes within the corresponding search grid. In (**a**,**b**,**d**,**e**), a red circle indicates the radiologist-annotated tumor location according to the mammogram; a magenta star indicates the location with the highest HbT in (**c**–**e**).

Tumor case study

A case study of a breast with a 10 mm diameter invasive ductal carcinoma (IDC) tumor from a 60 years old patient is shown in Fig. 8. The corresponding 2-D mammogram of the same breast, acquired 74 days prior to the optical scan, is shown in Fig. 8a along with a sample high-density optical diffuse transmittance image acquired using the EMCCD camera shown in Fig. 8b. A cross-sectional HbT plot of the compositional-prior-guided reconstruction[25] using sliding-bar illumination patterns and MLSVD-based detection patterns is shown in Fig. 8c and its superimposed with the co-registered mammogram is shown in Fig. 8d. The reconstruction residuals in diffuse transmittance over 10 iterations are shown in Fig. 8f. In Fig. 8, a red circle marks the tumor position suggested by the radiologist by reading the mammogram alone.

Comparing the HbT image recovered in Fig. 8c and the x-ray image in 8a, we notice that the highest HbT contrast, marked with a magenta star, does not align with the expected tumor location (red circle). One possible explanation of this misalignment is because the subject's breast was rotated slightly between the independent x-ray and OMCI compression procedures, despite that both were performed under the same MLO view. To verify this hypothesis, we apply a previously-validated tumor-prior scanning algorithm[28,29] to search for small and high-contrast inclusions in the vicinity of the tumor. Briefly, the tumor-prior scanning algorithm incorporates a 3-D Gaussian-spherical prior, representing the tumor tissue, as part of the regularization term[29], and places such hypothesized tumor prior across various locations within the breast. We found that when such a hypothesized tumor prior matches the true tumor location (concordant), the recovered HbT image show substantially increased contrast (ΔHbT for example) at the assumed tumor location; otherwise (discordant), ΔHbT only shows marginal changes[26,28]. This is best illustrated by a benchmark (Fig. 8) shown our previously published paper[26]. Using this distinctive behaviors of concordant and discordant tumor priors, we can perform a systematic search, seeking to localize small tumors without knowing its location in advance.

In this particular case, we use a Gaussian-sphere with a 10 mm FWHM as tumor prior and scan across a 6×6 grid spanning an area of 60×60 mm (black dotted area in Fig. 8e). For each search grid, we run a prior-guided reconstruction by placing the tumor-prior at the center of the grid. The difference (ΔHbT) between the recovered HbT with and without the tumor prior is computed and assigned to each grid. The resulting ΔHbT map after searching all 6×6 grid locations is shown in Fig. 8e. From our past clinical studies[28,29], the search grid cell reporting the highest ΔHbT usually aligns with the tumor's true location. From Fig. 8e, our tumor-search algorithm only identifies a single ΔHbT peak, which happens to match the location for the highest HbT value shown in Fig. 8c. Because that there is no other ΔHbT peak present in the vicinity of this region, we believe that the location coinciding with both the highest values of ΔHbT and HbT points to the tumor's actual location. This finding is in support of our earlier hypothesis that the breast was rotated between the x-ray and optical scans, and both of our recovered HbT and ΔHbT images are able to pinpoint the tumor's location.

Discussion

The OMCI system described in this work represents a promising step towards the integration of physiology-based tissue assessment into clinical breast cancer screening and care, providing a portable optical breast imaging system that can be used either in standalone DOT scans as well as used in conjunction with separately acquired mammography scans as part of the standard care. This "asynchronously multi-modal" breast DOT design not only potentially avoids the hurdles in regulatory approvals of vendor-specific integrated x-ray/DOT scanners, but also make optical breast assessment broadly available to tens of thousands of already-installed FFDM or DBT scanners worldwide, or even future new installations.

A key aspect in OMCI's design that enables convenient registration with clinical mammography scans is the design of the mechanical subsystem. It provides mammography-like compression so that the data from DOT and

x-ray acquired at the same mammography standard view can be "fused" to achieve better DOT reconstruction. Comparing to traditional fiber-optics based DOT systems developed by many groups[19,51–53], including our previous works[22,24,38], OMCI has dramatically improved the optical spatial sampling density, by adopting a projector-based area illumination and wide-field camera detector. This not only results in more spatially uniform sensitivity[36], but also the ability to increase source power by spreading across the entire illumination area without the risk of exceeding safety limit in fiber-based illumination.

Compared to a full-sized 20-detector-channel FD system we reported previously[38], the optical characterization of our miniaturized single-detector FD subsystem report a higher FD amplitude signal NEP of 6.0 pW/$\sqrt{Hz}$ compared to 1.4 pw/$\sqrt{Hz}$, as well as an elevated phase NEP of 10 mrad/$\sqrt{Hz}$ compared to 6 mrad/$\sqrt{Hz}$. We believe the increase of noise level could be attributed to reduced radio-frequency (RF) circuitry isolation and shielding due to use of a smaller form factor. However, the miniature FD subsystem reports a comparable dynamic ranges greater than 100 dB across both wavelengths.

The signal intensity and SNR plots shown in Fig. 5 strongly suggested that the choice of detection patterns do have a notable impact in the wide-field DOT measurement data quality. For example, when using MLSVD-optimized detection patterns, the average SNR at an EM gain of 20 is 72.3 dB, compared to the 66.4 dB produced by using the sliding-bar pattern at the same setting. We believe this increase of single-pixel data SNR is a result of more spatially distributed detection in the MLSVD patterns comparing to the relatively sparse sliding-bar patterns. This leads to increased detected total power and ultimately higher signal intensity and quality. Regardless, both sliding-bar and MLSVD-based single-pixel measurements from such wide-field DOT system exhibit dramatically more uniform signal SNR across all channels comparing to fiber-optics based DOT systems where an exponentially reduced SNR across source/detector separation is typically reported[22,53].

Using the example diffuse transmittance image captured by our camera detector, as shown in Figs. 3a and 8b, our wide-field DOT system clearly exhibits key advantages such as large field-of-view and high spatial sampling density comparing to other high-density DOT systems made of discrete sources and detectors[31,32]. Another key aspect we want to highlight here is the uniformity of light coupling and ease of image calibration comparing to optode-specific optical coupling that has been shown to be quite challenging to be removed[13,14]. Un-calibrated optode-specific coupling coefficients can result in localized artifacts that resembles the presence of tumors, leading to challenging image interpretation. A limitation of a camera-based detector is the relatively small dynamic range due to the limited bit-depth. However, this can be effectively compensated by dynamically adjusting EM gain to linearly scale the optical image to be within such range as well as the use of digital detection patterns to derive SP measurements with relatively uniform intensity, as shown in Fig. 5. We also want to note here that the ability to see superficial blood vessels in the optical measurements, which is previously not possible with fiber-based DOT systems, offers both new opportunities and challenges. In most of the breast reconstructions, these absorption features are limited to the superficial layers and do not "contaminate" the medial cross-sectional images of the breast as desired. This is a result of using 3-D measurements with limited z-axis resolution. However, we also notice that in some cases, superficial absorption features could extend to deeper slices of the breast, constituting an unwanted artifact. We believe a number of strategies we recently reported[36], such as truncation of patterns in addition to the use of x-ray priors could minimize such artifact.

Experimental validation using optical phantoms demonstrated that the OMCI system is capable of recovering deeply-embedded inclusions with breast tissue-like optical properties. In this case, the use of MLSVD-optimized detection patterns produced a relatively small (3%) improvement, as shown in Fig. 6d, compared to sliding-bar patterns. This is likely due to the simplicity of the tested phantom. In either case, the two inclusions were successfully recovered at the expected locations. Furthermore, as previously demonstrated[36], the enhanced recovered contrast and improved residual, indicating improved convergence to the underlying structure of the heterogeneous phantom described in Section 2.3, comes at no additional cost and is expected to work synergistically with other approaches for improving DOT image reconstruction, including prior-guided image reconstruction[17,54,55].

Our initial *in vivo* testing provided encouraging results regarding the potential clinical utility of the OMCI system. The recovered bulk properties averaged across 42 healthy breasts fall within the range of previously reported values[21,56]. Additionally, all reconstructed HbT images demonstrated general consistencies with the anatomical structures shown in the registered x-ray image slices; particularly, regions showing elevated HbT values generally overlap with the fibroglandular tissue or the axilla muscle, similar to those observed in our previous studies[21]. Comparing the recovered imaging contrasts between the 2nd and 3rd columns, as well as the residual plots in the last column of Fig. 7, we see that the use of MLSVD-derived detection patterns further enhances the tissue contrasts while reducing the diffuse transmittance residual ranging between 3% to 6% at the 10th reconstruction iteration. These findings further affirm the observations we made recently[36], wherein a medium-adaptive pattern set is shown to yield improved image sharpness, reconstruction contrast, and reduced background noise. This result also further highlights that while WF techniques offer numerous advantages as previously described, fully leveraging the wealth of information acquired may require advanced data processing techniques, for example, optimized scanning patterns.

Comparing recovered HbT images in the 4th/5th columns against those in the 2nd/3rd columns in Fig. 7, the use of x-ray derived compositional priors[25,30] significantly improved the spatial details of the DOT images, showing more subtle structures that were not visible in the non-prior-guided reconstructions. The use of priors also allow reliable recovery of the the axilla muscle regions, which were expected to have higher HbT content, at the top corner regions of the 2nd and 3rd breasts. Based on the residual plots on the last column, the use of structural-priors generally resulted in a slight decrease in diffuse transmittance residual, suggesting that the prior-guided reconstructions not only produce sharper images, but also fit the measurement data better. It is worth highlighting that the compositional prior is applied as a "soft-constraint", and permits the optical measurements to drive image contrast recovery without being forced by the x-ray prior. This is particularly useful as not only do

the HbT and x-ray contrasts reflect two different properties (physiological and morphological, respectively) of breast tissues, but also the x-ray information was asynchronously acquired, and thus the tissue structures in the x-ray may not match their positions in the optical data.

The ability to consider misaligned spatial prior knowledge is further demonstrated in the following tumor case study. Here, a breast with a 10 mm diameter IDC [Fig. 8] has been imaged. Although the overall spatial distribution of the reconstructed HbT [Fig. 8c] resembles the fibroglandular regions shown in the mammogram [Fig. 8a], the location of the highest recovered HbT (magenta star) does not overlap with the tumor location (red circle) identified by the radiologist. We hypothesized that this might have been caused by the inconsistent breast positioning between the independent x-ray and optical compressions. By applying a tumor-scanning DOT reconstruction algorithm[28,29], which has a known capability of localizing small and high-contrast inclusions such as a tumor, we discovered that the highest ΔHbT (13.2 μM) recovered by the tumor-scanning algorithm [Fig. 8e] overlaps with the highest HbT location in the DOT reconstructed image, confirming that a small high-contrast inclusion, likely the IDC after breast rotation, appears at the HbT peak location. In comparison, marginal changes are observed in the annotated tumor region (ΔHbT = 0.57 μM). The implications of such a finding are two-fold. First, it shows that our wide-field DOT reconstruction has the capability to recover malignant tumors, either conventional optical reconstructions, for example, using HbT contrast, or ΔHbT derived from the tumor-scanning algorithm. Previous works[28,29] have also demonstrated that the tumor-prior scanning technique may have a background suppression effect, with a low recovered ΔHbT value in incorrectly positioned tumor-prior locations, leading to significantly enhanced tumor contrast in this differential map. Second, it also demonstrates the possibility of misalignment between separately acquired x-ray and optical scans even performed under the same mammography view. As previously mentioned, our compositional-prior-guided DOT reconstructions[25] applies the structural prior in the form of "soft" constraints, making it possible to recover breast tumors even when the x-ray prior is inaccurate.

Despite the various advances demonstrated in the above results, the current design of the OMCI breast imaging system has room to be further improved in our future works. First of all, the current source illumination area, $11\times6\ \mathrm{cm}^2$, is relatively small compared to the large field-of-view ($\sim16\times16\ \mathrm{cm}^2$) captured from the camera detector. We hope to further enlarge the illumination area by modifying the coupling optics so that the sensitivity on the source side can be expanded to the full contact area of the breast. This also requires us to correspondingly increase the CW source laser power as we enlarge the illumination area. Secondly, the relatively small number of FD data points in OMCI data are used largely for bulk property estimation. It is possible to re-design the mount for the dual-axis galvonometer to significantly increase the FD scanning density, including a 2-D scanning pattern. The additional FD measurements could aid the spatial recovery of optical images. Thirdly, the current OMCI design only includes two wavelengths with the primary focus of recovering HbO/HbR images. It has been previously reported that additional tissue chromophores, such as water and collagen content, could also help clinical diagnosis of breast cancer[57–59]. Because of the frequency-encoding design, our FD system can potentially incorporate more wavelengths without extending scanning time[60,61]. Finally, in our on-going clinical study, we are continue expanding our *in vivo* measurements using OMCI from breasts with malignant and benign lesions. We will further analyze and compare these results and assess the ability to distinguish between lesion types in conjunction with mammography based diagnosis.

Conclusion

We have developed a portable, wide-field, ultra-high-density DOT-based optical breast imaging system (OMCI) that has the potential to bring functional assessment of breast tissues to widely available digital mammography and DBT systems across the world. The OMCI is capable of taking DOT scan of a breast while applying mammography-like compression; this allows one to jointly use the structural information obtained from separately acquired clinical mammography scans with the optical data reconstruction, producing substantially improved image quality and spatial details compared to standalone DOT images. The use of pattern illumination based area sources and camera-based wide-field detectors makes it possible to scan the breast optically with a spatial density (in terms of raw channel counts) several orders of magnitude higher than fiber-optics based HD-DOT systems while the use of compressive image reconstruction[36] still yields a compact inverse problem that can be solved computationally efficiently. Further development and testing of this unique breast DOT system could lead to clinical translation of multi-modal DOT in breast cancer diagnosis and ultimately improve the clinical management of breast cancers.

Data availability

The data that support the findings of this study are not openly available due to reasons of sensitivity; however, example datasets as well as the processing codes are available from the corresponding author upon reasonable request. Data are located in controlled access data storage at Northeastern University.

Received: 26 September 2024; Accepted: 26 February 2025
Published online: 13 March 2025

References

1. Siegel, R. L., Giaquinto, A. N. & Jemal, A. Cancer statistics, 2024. *CA Cancer J. Clin.* **74**, 12–49. https://doi.org/10.3322/caac.21820 (2024).
2. Caswell-Jin, J. L. et al. Analysis of Breast Cancer Mortality in the US - 1975 to 2019. *JAMA* **331**, 233–241. https://doi.org/10.1001/jama.2023.25881 (2024).
3. Pisano, E. D. & Yaffe, M. J. *Digital mammography*[SPACE]https://doi.org/10.1148/radiol.2342030897 (2005).

4. Chong, A., Weinstein, S. P., McDonald, E. S. & Conant, E. F. *Digital breast tomosynthesis: Concepts and clinical practice*[SPACE]https://doi.org/10.1148/radiol.2019180760 (2019).
5. Guo, R., Lu, G., Qin, B. & Fei, B. *Ultrasound imaging technologies for breast cancer detection and management: A review*[SPACE]https://doi.org/10.1016/j.ultrasmedbio.2017.09.012 (2018).
6. Ho, T. Q. H. et al. Cumulative probability of false-positive results after 10 years of screening with digital breast tomosynthesis vs digital mammography. *JAMA Netw. Open* **5**, E222440. https://doi.org/10.1001/jamanetworkopen.2022.2440 (2022).
7. Mann, R. M., Kuhl, C. K. & Moy, L. *Contrast-enhanced mri for breast cancer screening*[SPACE]https://doi.org/10.1002/jmri.26654 (2019).
8. Eubank, W. B. & Mankoff, D. A. Evolving role of positron emission tomography in breast cancer imaging. *Semin. Nucl. Med.* **35**, 84–99. https://doi.org/10.1053/j.semnuclmed.2004.11.001 (2005).
9. Dodelzon, K., McGinty, G. & Melsaether, A. PET/MRI in breast cancer patients: added value, barriers to implementation, and solutions. https://doi.org/10.1016/j.clinimag.2020.06.002 (2020).
10. Leff, D. R. et al. Diffuse optical imaging of the healthy and diseased breast: A systematic review. *Breast Cancer Res. Treat.* **108**, 9–22. https://doi.org/10.1007/s10549-007-9582-z (2008).
11. Busch, D. R., Choe, R., Durduran, T. & Yodh, A. G. Toward noninvasive characterization of breast cancer and cancer metabolism with diffuse optics. *PET Clin.* **8**, 345–365. https://doi.org/10.1016/j.cpet.2013.04.004 (2013) arXiv:NIHMS150003.
12. Arridge, S. R. & Schotland, J. C. Optical tomography: forward and inverse problems. *Inverse Problems* **25**, 123010. https://doi.org/10.1088/0266-5611/25/12/123010 (2009).
13. Boas, D., Gaudette, T. & Arridge, S. Simultaneous imaging and optode calibration with diffuse optical tomography. *Opt. Express* **8**, 263. https://doi.org/10.1364/OE.8.000263 (2001).
14. Schweiger, M., Nissilä, I., Boas, D. A. & Arridge, S. R. Image reconstruction in optical tomography in the presence of coupling errors. *Appl. Opt.* **46**, 2743. https://doi.org/10.1364/AO.46.002743 (2007).
15. Durduran, T., Choe, R., Baker, W. B. & Yodh, A. G. Diffuse optics for tissue monitoring and tomography. *Rep. Prog. Phys.* **73**, 076701. https://doi.org/10.1088/0034-4885/73/7/076701 (2010).
16. El-Ghussein, F., Mastanduno, M. A., Jiang, S., Pogue, B. W. & Paulsen, K. D. Hybrid photomultiplier tube and photodiode parallel detection array for wideband optical spectroscopy of the breast guided by magnetic resonance imaging. *J. Biomed. Opt.* **19**, 011010. https://doi.org/10.1117/1.JBO.19.1.011010 (2013).
17. Ntziachristos, V., Yodh, A., Schnall, M. D. & Chance, B. MRI-guided diffuse optical spectroscopy of malignant and benign breast lesions. *Neoplasia* **4**, 347–354. https://doi.org/10.1038/sj.neo.7900244 (2002).
18. Feng, J., Jiang, S., Pogue, B. W. & Paulsen, K. D. Performance assessment of mri guided continuous wave near-infrared spectral tomography for breast imaging. *Biomed. Opt. Express* **12**, 7657. https://doi.org/10.1364/boe.444131 (2021).
19. Cochran, J. M. et al. Hybrid time-domain and continuous-wave diffuse optical tomography instrument with concurrent, clinical magnetic resonance imaging for breast cancer imaging. *J. Biomed. Opt.* **24**, 1. https://doi.org/10.1117/1.jbo.24.5.051409 (2019).
20. Zhu, Q. et al. Early-stage invasive breast cancers: Potential role of optical tomography with US localization methods: Results. *Radiology* **256**, 367–378. https://doi.org/10.1148/radiol.10091237/-/DC1 (2010).
21. Fang, Q. et al. Combined optical and x-ray tomosynthesis breast imaging. *Radiology* **258**, 89–97. https://doi.org/10.1148/radiol.10082176 (2011).
22. Zimmermann, B. B. et al. Multimodal breast cancer imaging using coregistered dynamic diffuse optical tomography and digital breast tomosynthesis. *J. Biomed. Opt.* **22**, 046008. https://doi.org/10.1117/1.JBO.22.4.046008 (2017).
23. Zhang, Q. et al. Coregistered tomographic x-ray and optical breast imaging: initial results. *J. Biomed. Opt.* **10**, 024033. https://doi.org/10.1117/1.1899183 (2005).
24. Fang, Q. et al. Combined optical imaging and mammography of the healthy breast: Optical contrast derived from breast structure and compression. *IEEE Trans. Med. Imaging* **28**, 30–42. https://doi.org/10.1109/TMI.2008.925082 (2009).
25. Fang, Q., Moore, R. H., Kopans, D. B. & Boas, D. A. Compositional-prior-guided image reconstruction algorithm for multi-modality imaging. *Biomed. Opt. Express* **1**, 223. https://doi.org/10.1364/boe.1.000223 (2010).
26. Deng, B., Brooks, D. H., Boas, D. A., Lundqvist, M. & Fang, Q. Characterization of structural-prior guided optical tomography using realistic breast models derived from dual-energy x-ray mammography. *Biomed. Opt. Express* **6**, 2366. https://doi.org/10.1364/boe.6.002366 (2015).
27. Deng, B., Lundqvist, M., Fang, Q. & Carp, S. A. Impact of errors in experimental parameters on reconstructed breast images using diffuse optical tomography. *Biomed. Opt. Express* **9**, 1130. https://doi.org/10.1364/boe.9.001130 (2018).
28. Muldoon, A. et al. Method to improve the localization accuracy and contrast recovery of lesions in separately acquired x-ray and diffuse optical tomographic breast imaging. *Biomed. Opt. Express* **13**, 5295. https://doi.org/10.1364/boe.470373 (2022).
29. Fang, Q. Method to localize small and high contrast inclusions in ill-posed model-based imaging modalities. U.S. patent US 11,246,529 B2 (2022).
30. Deng, B. et al. Characterizing breast lesions through robust multimodal data fusion using independent diffuse optical and x-ray breast imaging. *J. Biomed. Opt.* **20**, 080502. https://doi.org/10.1117/1.JBO.20.8.080502 (2015).
31. Wheelock, M. D., Culver, J. P. & Eggebrecht, A. T. High-density diffuse optical tomography for imaging human brain function. *Rev. Sci. Instrum.*[SPACE]https://doi.org/10.1063/1.5086809 (2019).
32. Chitnis, D. et al. Functional imaging of the human brain using a modular, fibre-less, high-density diffuse optical tomography system. *Biomed. Opt. Express* **7**, 4275. https://doi.org/10.1364/boe.7.004275 (2016).
33. Chen, J., Venugopal, V., Lesage, F. & Intes, X. Time-resolved diffuse optical tomography with patterned-light illumination and detection. *Opt. Lett.* **35**, 2121. https://doi.org/10.1364/OL.35.002121 (2010).
34. Escobet-Montalbán, A. et al. Wide-field multiphoton imaging through scattering media without correction. *Science Adv.*[SPACE]https://doi.org/10.1126/sciadv.aau1338 (2018).
35. Bai, W. et al. Wide-field illumination diffuse optical tomography within a framework of single-pixel time-domain spatial frequency domain imaging. *Opt. Express* **32**, 6104. https://doi.org/10.1364/OE.513909 (2024).
36. Mireles, M., Xu, E., Ragunathan, R. & Fang, Q. Medium-adaptive compressive diffuse optical tomography. *Biomed. Opt. Express* **15**, 5128–5142. https://doi.org/10.1364/BOE.529195 (2024).
37. Angelo, J. P. et al. Review of structured light in diffuse optical imaging. *J. Biomed. Opt.* **24**, 071602. https://doi.org/10.1117/1.JBO.24.7.071602 (2018).
38. Zimmermann, B. B., Fang, Q., Boas, D. A. & Carp, S. A. Frequency domain near-infrared multiwavelength imager design using high-speed, direct analog-to-digital conversion. *J. Biomed. Opt.* **21**, 1–8. https://doi.org/10.1117/1.JBO.21.1.016010 (2016).
39. Yao, R., Pian, Q. & Intes, X. Wide-field fluorescence molecular tomography with compressive sensing based preconditioning. *Biomed. Opt. Express* **6**, 4887. https://doi.org/10.1364/BOE.6.004887 (2015).
40. Bélanger, S., Abran, M., Intes, X., Casanova, C. & Lesage, F. Real-time diffuse optical tomography based on structured illumination. *J. Biomed. Opt.* **15**, 016006. https://doi.org/10.1117/1.3290818 (2010).
41. Vanegas, M., Mireles, M., Xu, E., Yan, S. & Fang, Q. Compact breast shape acquisition system for improving diffuse optical tomography image reconstructions. *Biomed. Opt. Express* **14**, 1579–1593. https://doi.org/10.1364/BOE.481092 (2023).
42. Sansoni, G., Corini, S., Lazzari, S., Rodella, R. & Docchio, F. Three-dimensional imaging based on gray-code light projection: characterization of the measuring algorithm and development of a measuring system for industrial applications. *Appl. Opt.* **36**, 4463–4472. https://doi.org/10.1364/AO.36.004463 (1997).

43. Fang, Q. *et al.* A multi-modality image reconstruction platform for diffuse optical tomography. In *Biomedical Optics*, BMD24, https://doi.org/10.1364/BIOMED.2008.BMD24 (OSA, Washington, D.C., 2008).
44. Moreno, D. & Taubin, G. Simple, accurate, and robust projector-camera calibration. In *Proceedings - 2nd Joint 3DIM/3DPVT Conference: 3D Imaging, Modeling, Processing, Visualization and Transmission*, 464–471, https://doi.org/10.1109/3DIMPVT.2012.77 (IEEE, 2012).
45. Kazhdan, M., Bolitho, M. & Hoppe, H. Poisson surface reconstruction (2006).
46. Fang, Q. & Boas, D. A. Tetrahedral mesh generation from volumetric binary and grayscale images. In *2009 IEEE International Symposium on Biomedical Imaging: From Nano to Macro*, vol. 19, 1142–1145, https://doi.org/10.1109/ISBI.2009.5193259 (IEEE, 2009).
47. Tran, A. P., Yan, S. & Fang, Q. Improving model-based functional near-infrared spectroscopy analysis using mesh-based anatomical and light-transport models. *Neurophotonics* **7**, 1. https://doi.org/10.1117/1.NPh.7.1.015008 (2020).
48. Chetverikov, D., Svirko, D. & Stepanov, D. The trimmed iterative closest point algorithm.
49. Gibson, G. M., Johnson, S. D. & Padgett, M. J. Single-pixel imaging 12 years on: a review. *Opt. Express* **28**, 28190. https://doi.org/10.1364/OE.403195 (2020).
50. Hansen, P. C. & O'Leary, D. P. The use of the l-curve in the regularization of discrete ill-posed problems. *SIAM J. Sci. Comput.* **14**, 1487–1503. https://doi.org/10.1137/0914086 (1993).
51. McBride, T. O. et al. Multispectral near-infrared tomography: a case study in compensating for water and lipid content in hemoglobin imaging of the breast. *J. Biomed. Opt.* **7**, 72–9. https://doi.org/10.1117/1.1428290 (2002).
52. Chae, E. Y. et al. Development of digital breast tomosynthesis and diffuse optical tomography fusion imaging for breast cancer detection. *Sci. Rep.* **10**, 13127. https://doi.org/10.1038/s41598-020-70103-0 (2020).
53. Krishnaswamy, V. et al. A digital x-ray tomosynthesis coupled near infrared spectral tomography system for dual-modality breast imaging. *Opt. Express* **20**, 19125. https://doi.org/10.1364/OE.20.019125 (2012).
54. Yalavarthy, P. K. et al. Structural information within regularization matrices improves near infrared diffuse optical tomography. *Opt. Express* **15**, 8043–8058. https://doi.org/10.1364/OE.15.008043 (2007).
55. Althobaiti, M., Vavadi, H. & Zhu, Q. Diffuse optical tomography reconstruction method using ultrasound images as prior for regularization matrix. *J. Biomed. Opt.* **22**, 26002 (2017).
56. Durduran, T. et al. Bulk optical properties of healthy female breast tissue. *Phys. Med. Biol.* **47**, 302. https://doi.org/10.1088/0031-9155/47/16/302 (2002).
57. Shah, N. et al. The role of diffuse optical spectroscopy in the clinical management of breast cancer. *Dis. Markers* **19**, 95–105. https://doi.org/10.1155/2004/460797 (2004).
58. Cerussi, A. et al. In vivo absorption, scattering, and physiologic properties of 58 malignant breast tumors determined by broadband diffuse optical spectroscopy. *J. Biomed. Opt.* **11**, 044005. https://doi.org/10.1117/1.2337546 (2006).
59. Taroni, P. et al. Non-invasive optical estimate of tissue composition to differentiate malignant from benign breast lesions: A pilot study. *Sci. Rep.* **7**, 40683. https://doi.org/10.1038/srep40683 (2017).
60. Applegate, M. B. & Roblyer, D. High-speed spatial frequency domain imaging with temporally modulated light. *J. Biomed. Opt.* **22**, 076019. https://doi.org/10.1117/1.JBO.22.7.076019 (2017).
61. Xu, E., Mireles, M., Carp, S. & Fang, Q. Combined intensity- and spatially-modulated widefield diffuse optical tomography. In *Biophotonics Congress: Biomedical Optics 2022 (Translational, Microscopy, OCT, OTS, BRAIN)*, JM3A.16. https://doi.org/10.1364/TRANSLATIONAL.2022.JM3A.16 (Optica Publishing Group, 2022).

Acknowledgements

This work was developed with funding from the National Institutes of Health under grants No. R01-CA204443 and No. R01-GM114365. The authors acknowledge Aiza Kabeer and Joyce Chu for their assistance in coordinating our clinical studies.

Author contributions

Q.F. conceived the OMCI system; M.M., E.X., M.V., S.C and Q.F. designed, and validated the OMCI system. M.M., E.X., M.V. and R.R. built the hardware for OMCI. M.M., E.X., M.V., and Q.F. wrote the controlling and acquisition software for the auxiliary and optical subsystems. M.M., E.X., M.V., R.R. and S.Y. developed and assessed the data processing workflow. S.C. and Q.F. conceived and wrote the clinical trials protocols. M.M., E.X., M.V., R.R., and Q.F. conceived the experiments. M.M., E.X., M.V. and R.R conducted the validation experiments. Clinical trials were performed by A.M., B.D., and J.C. at Massachusetts General Hospital-Danvers. M.S. provided clinical guidance and interpretation of mammography images. M.M. and E.X. analyzed the clinical data. All authors reviewed the manuscript.

Declarations

Competing interests

The authors declare no competing interests.

Additional information

Correspondence and requests for materials should be addressed to Q.F.

Reprints and permissions information is available at www.nature.com/reprints.

Publisher's note Springer Nature remains neutral with regard to jurisdictional claims in published maps and institutional affiliations.